15th World Congress on Computational Mechanics (WCCM-XV)
8th Asian Pacific Congress on Computational Mechanics (APCOM-VIII)
Virtual Congress: 31 July – 5 August 2022
S. Koshizuka (Ed.)

CLARIFICATION OF THE DAMAGE MECHANISM OF THE LONG-PERIOD BRIDGE SYSTEM DAMAGED BY THE 2016 KUMAMOTO EARTHQUAKE

SHOGO YAMAMOTO[1], GAKU SHOJI[2] AND MICHIO OHSUMI[3]

[1] University of Tsukuba
1-1-1, Tennodai, Tsukuba, Ibaraki 305-8573 Japan
yamamoto.shogo.su@alumni.tsukuba.ac.jp

[2] University of Tsukuba
1-1-1, Tennodai, Tsukuba, Ibaraki 305-8573 Japan
gshoji@kz.tsukuba.ac.jp

[3] Public Works Research Institute
1-6, Minamihara, Tsukuba, Ibaraki 305-8516 Japan
m-oosumi@pwri.go.jp

Key words: Long-Period Bridge System, 3D FE Model, 2016 Kumamoto Earthquake

Abstract. *This study aims to clarify the damage mechanism of a long-period bridge system—the Ohkirihata Bridge damaged in the 2016 Kumamoto earthquake— subjected to the combined effects of long-period pulsive ground motions and surface fault displacements. The target bridge's site-specific waveforms at abutment A1 were estimated using the finite difference method. Linear dynamic analysis with a three-dimensional finite element model of the bridge structure-underground interconnected system was performed to examine the effects of long-period pulsive ground motions on the coupled responses of essential structural components: superstructure, rubber bearings, abutments, piers, foundations and underground.*

1 INTRODUCTION

In April 2016, the Kumamoto earthquake occurred due to an active fault in the Hutagawa–Hinagu fault zone near Kumamoto Prefecture in Japan. Two earthquakes measuring 7 on the Japanese seismic intensity scale occurred on 14 and 16 April, with magnitudes of 6.5 and 7.3, respectively[1].

Surface fault displacements were observed near the Ohkirihata Bridge, a typical example of a long-period bridge system. The combined effects of the loads with long-period pulsive ground motions seem to cause extensive damage to the Ohkirihata Bridge. However, it is unclear which combined effects contributed to the damage to specific structural elements. The damage to the Ohkirihata Bridge included the movement of girders of about 1 m, cracks in the pier columns and slabs and residual displacement of 20–50 cm in each pier concerning abutments[2][3]. In addition, laminated rubber bearings (RBs) on all piers and abutments were damaged. The laminated RBs were ruptured on the abutments, residual displacement was visible on pier P2,

shear keys dislodged, and mounting bolts were broken on piers except for pier P2[2][3]. This damage caused successively residual displacements of the girders on abutments and piers.

This study aims to clarify the damage mechanism of a long-period bridge structure-underground interconnected system—the Ohkirihata Bridge damaged in the 2016 Kumamoto earthquake—subjected to the combined loads of long-period pulsive ground motions and surface fault displacements. After estimating site-specific waveforms near the Ohkirihta Bridge in the Kumamoto earthquake, they are applied to a three-dimensional (3D) finite element (FE) model of the bridge structure-underground interconnected system. The discussion focuses on the effects of long-period pulsive ground motions on the dynamic behaviours of the superstructure supported by the laminated RBs and the substructures.

2 ESTIMATION OF SITE-SPECIFIC WAVEFORMS

We estimated the site-specific waveforms on the engineering base surface under the Ohkirihata Bridge using the finite difference (FD) method with fourth-order spatial and second-order temporal discretization[4]. The following is a detailed description of our analysis.

2.1 Earthquake source fault model and underground structure

We applied the earthquake source fault model of Asano and Iwata[5]. The starting time for the earthquake set in this model was 1:25:5.47 am on 16 Apr 2016, and the location of the hypocenter was 32.7545°N, 130.7630°E, at a 12.45-km depth, which was specified by the Japan Meteorological Agency, JMA[1]. The model comprises two faults—the Hinagu and Hutagawa Faults—and sub-faults were idealized as 63 point sources with nine rows and seven columns and as 126 those with nine rows and 14 columns, respectively. The angles of the fault line from the north direction were 205° and 235°, respectively, and the dip angles were 72° and 65°, respectively. The source time function was modelled by summing nine 1-s-wide smoothed ramp functions at 0.5-s intervals for each sub-fault.

We used the underground structure of 23 layers, which Hara[6] modelled based on the underground structure data of the Headquarters for Earthquake Research Promotion[7].

2.2 Calculational region and numerical conditions

We applied the computational region, including the absorption region, which was 89.4 km north-south (NS) × 79.2 km east-west (EW) × 40 km up and down (UD), which Hara[6] similarly modelled. The computational region was divided vertically into two parts, with the shallow area above the boundary as Region I and the deep area below as Region II. The boundary between Region I and Region II was 22-km deep. The upper frequency was 0.5 Hz, and the grid sizes of Regions I and II were $100 \times 100 \times 100$ and $300 \times 300 \times 300$ m^3, respectively, for the stability of the FD calculation. The time step was 0.005 sec, and the computation time was 50 sec.

2.3 Calculation results

Figure 1 shows the estimated velocity and acceleration waveforms of the site-specific waveforms near abutment A1 of the Ohkirihata Bridge. From Figure 1, the maximum velocity

is about 0.80 and 0.89 m/s for EW and NS, respectively, and the maximum acceleration is about 5.1 and 7.2 m/s² for EW and NS, respectively, indicating that the ground motion is particularly large in the NS direction.

Figure 2 shows the acceleration and displacement response spectra. The damping constant is assumed to be 0.05. Figure 2 also shows the standard acceleration response spectrum of Type II design ground motion for Type II ground[8] and the first natural period of 1.20 s of the Ohkirihata Bridge obtained by eigenvalue analysis based on the 3D FE model considering the interaction between the structure and the surrounding ground[9]. At 1.2 sec, the first natural period of the Ohkirihata Bridge, the response acceleration is 8.7 and 10.7 m/s² for EW and NS, respectively, which is not large. However, the response displacement is 0.32 and 0.39 m for EW and NS, respectively, almost the peak response displacement. Therefore, pulses from fault ruptures contributed significantly to the response displacement of the Ohkirihata Bridge.

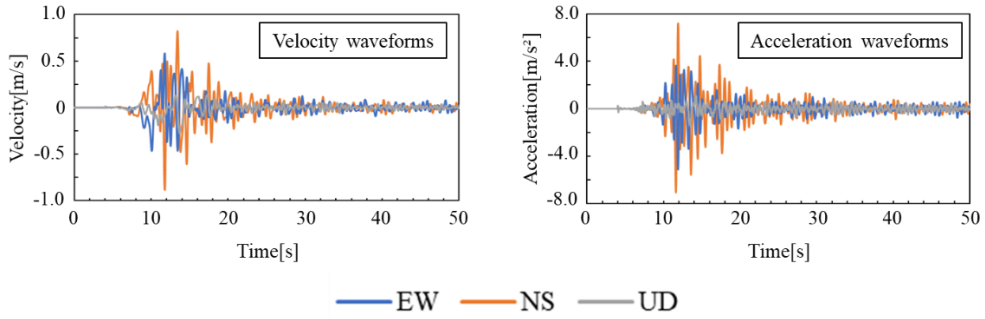

Figure 1: Estimated velocity and acceleration waveforms of site-specific waveforms near abutment A1

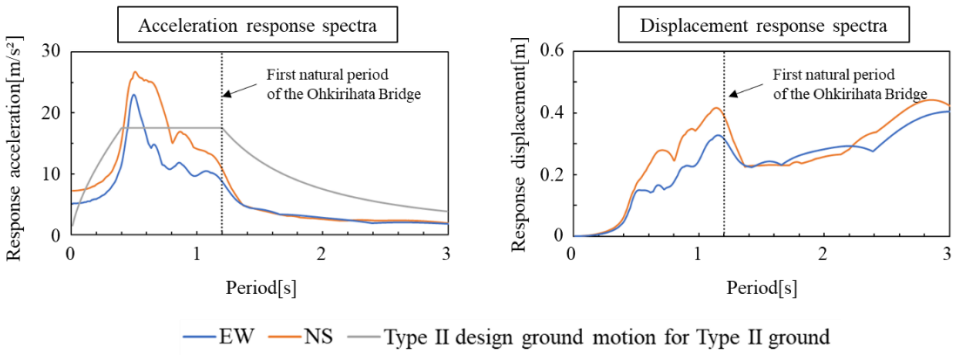

Figure 2: Response spectra of site-specific waveforms

3 TARGET BRIDGE FOR ANALYSIS

The Ohkirihata Bridge is a 5-span continuous steel plate girder bridge of 265.4-m long, 12.5-m wide, located on Kumamoto Prefectural Road 28. Figure 3 shows a 3D computer-aided design model of the bridge structure-underground interconnected system of the Ohkirihata Bridge, which was created based on the general drawings of the bridge and design documents by Kumamoto Reconstruction Project Office. Each structural element of the bridge is described in detail below.

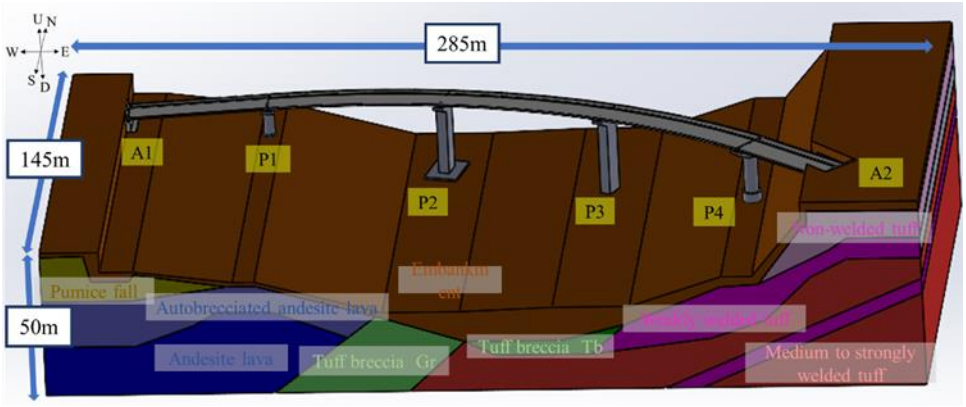

Figure 3: 3D computer-aided design model of bridge structure-underground interconnected system

3.1 Superstructure

The superstructure of the Ohkirihata Bridge comprises the five main girders which have a girder height of 2,600 mm and a web thickness of 11 mm. The width and thickness of the flanges vary depending on their location, in the range of 330–760 and 16–36 mm, respectively. On top of the girders, reinforced concrete (RC) slabs with a 220-mm thickness are set. The superstructure curve from pier P1 to abutment A2.

Bridge fall prevention cables with a diameter of 24.3 mm are at abutments A1 and A2, two on each main girder.

3.2 Laminated rubber bearings

Laminated RBs support the Ohkirihata Bridge and are installed on each abutment and pier, corresponding to each of the five main girders. The laminated RBs on abutment A1 have an effective pressure area of 450 × 450 mm^2 with 10 layers of natural rubber of a 12-mm thickness and nine layers of internal steel plates, whereas those on abutment A2 have an effective pressure area of 500× 500 mm^2 with eight layers of natural rubber of a 15-mm thickness and seven layers of internal steel plates. The RBs on pier P1 have an effective pressure area of 650× 650 mm^2 with 10 layers of natural rubber of a 15-mm thickness and nine layers of internal steel plates. The RBs on piers P2 and P3 have an effective pressure area of 650× 650 mm^2 with five layers of natural rubber of a 17-mm thickness and four layers of internal steel plates. The RBs on pier P4 have an effective pressure area of 650 × 650 mm^2 with 10 layers of natural rubber of a 14-mm thickness and nine layers of internal steel plates. The thickness of each internal steel plate is 3 mm, and the thickness of each upper and lower steel plate is 25 mm.

3.3 Abutments, piers and foundations

Abutment A1 is an inverted-T RC abutment with eight cast-in-place piles of 1,200-mm diameter and 17-m long. Abutment A2 is also an inverted-T RC abutment with two caisson piles of 2,000-mm diameter and 11- and 7-m long. Piers P1 and P4 are overhanging T-shaped circular RC piers with the height of 10 m and 16 m, respectively. They have the foundations of caisson piles with diameters of 4,500 and 6,000 mm, and lengths of 15 and 30 m, respectively. Piers P2 and P3 are overhanging T-shaped rectangular RC piers with the height of 24.5 and 30

m, respectively. They have the foundations of cast-in-place piles with 10 and 12 piles, respectively, of 1,500-mm diameter. Pier P1 has the solid section. Piers P2, P3 and P4 have the solid section from the bottom of each column to 3.5 m, and the hollow section from 3.5 m to the top of each column.

3.4 Underground

Figure 3 also shows the underground structure at the Ohkirihata Bridge, which comprises nine soil layers. The engineering base is identified as the andesite lava, which is located in the depth of 50 m from the surface ground of abutment A1. The pumice fall, autobrecciated andesite lava, andesite lava and tuff breccia are ejecta of the Ohmine Volcano deposited around abutment A1. The non-welded tuff, weakly welded tuff, and medium to strongly welded tuff are the Aso pyroclastic-flow deposits deposited around abutment A2.

4 ANALYSIS MODEL OF TARGET BRIDGE

4.1 3D FE model of bridge structure-underground interconnected system

The superstructure, abutments, piers, foundations, and underground were modelled with tetrahedral first-order elements. The underground is 285, 145 and 50 m in the EW, NS and UD directions. A layer of natural rubber and steel plate was modelled by a hexahedral first-order element. All structural elements are assumed to be isotropic materials. The nodes of the elements between the foundations and underground were linked to each other. The expansion joints and bridge fall prevention cables were not modelled in this analysis. This analysis will not consider friction and slip behaviours between the foundations and underground. Finally, the 3D FE model of the bridge structure-underground interconnected system of the Ohkirihata Bridge was constructed, as shown in Figure 4. The numbers of nodes and elements are 441,196 and 2,437,126, respectively. The boundary conditions of the surrounding underground and bottom were set to be completely fixed.

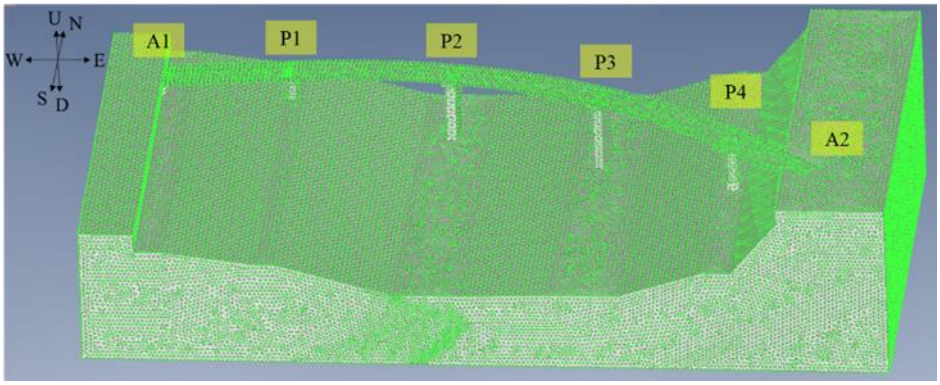

Figure 4: 3D FE model of bridge structure-underground interconnected system of Ohkirihata Bridge

4.2 Material constitutive laws and material properties

The superstructure was modelled as a solid element by combining the stiffnesses of the bridge girders with the slab model. The combined Young's modulus is calculated, as shown in

Figure 5. In Figure 5(a), the superstructure is simplified to comprise a slab and five main girders, not considering cross beams, lateral bracings and sway bracings . The cross-sectional area of the slab and the average cross-sectional area of each main girder are calculated from the design documents. Next, the average cross-sectional area of each main girder is summed as in Figure 5(b), and the main girders are modelled as an equivalent rectangular cross-sectional element with the area of 0.248 m². We calculate the composite Young's modulus of the slab and main girders in the direction of the bridge axis E' using the volume ratio of the slab V_R, Young's modulus of RC E_R, volume ratio of the main girders V_S and Young's modulus of steel E_S. Finally, as in Figure 5(c), we combined the stiffness of the main girders with the model of the slab.

Table 1 shows the Young's modulus of the superstructure. This Young's modulus was applied isotropically, and the superstructure was assumed to be a linear elastic body. The density of the superstructure in unit mass shown in Table 1 was calculated as 4.910×10^3 kg/m^3 by using the density in a unit length of 1.505×10^4 kg/m based on the design documents.

To reveal dynamic elastic responses for interconnected structure elements, all structural elements, such as bearings, abutments, piers, foundations and underground are assumed to be a linear elastic body. Table 1 shows the material properties of density, Young's modulus and Poisson's ratio of each structural elements.

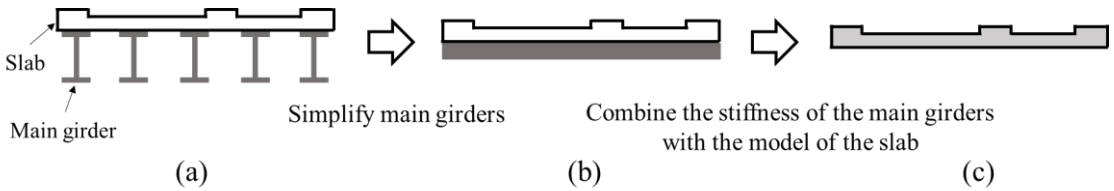

Figure 5: Method for calculating Young's modulus of the superstructure

Table 1: Material properties of each structural element

	Density [kg/m³]	Young's modulus [N/m²]	Poisson's ratio
Superstructure	4,910	4.1×10^{10}	0.2
Abutments・Piers・Foundations	2,400	2.4×10^{10}	0.2
Natural rubber	910	2.92×10^{6}	0.49
Steel	7,850	2.05×10^{11}	0.3
Embankment	1,735	8.4×10^{6}	0.4
Pumice fall	1,530	1.1×10^{6}	0.4
Tuff breccia Gr	2,142	3.9×10^{7}	0.4
Tuff breccia Tb	2,142	5.2×10^{7}	0.4
Autobrecciated andesite lava	1,428	2.8×10^{7}	0.4
Andesite lava	2,142	1.1×10^{8}	0.4
Non-welded tuff	2,142	1.4×10^{7}	0.4
Weakly welded tuff	2,142	4.7×10^{7}	0.4
Medium to strong welded tuff	2,346	1.8×10^{8}	0.4

5 ANALYSIS CONDITIONS

We used an open-source programme for large-scale parallel computation of FE analysis: FrontISTR[10]. Linear dynamic analysis was performed by applying the acceleration waveforms as equivalent inertial forces in the EW, NS and UD directions to all nodes of the 3D FE model shown in Figure 4. The acceleration waveforms of the site-specific waveforms shown in Figure 1 were used as the input waves, and the waveforms were applied for 18 sec from 0 to 18 sec in 50-sec duration.

The equation of motion to be solved in linear dynamic analysis is given by

$$\boldsymbol{M}\ddot{\boldsymbol{U}}(t) + \boldsymbol{C}\dot{\boldsymbol{U}}(t) + \boldsymbol{K}\boldsymbol{U}(t) = \boldsymbol{F} \tag{1}$$

where $\boldsymbol{M}$ is the mass matrix, $\ddot{\boldsymbol{U}}(t)$ is the acceleration vector, $\boldsymbol{C}$ is the damping matrix, $\dot{\boldsymbol{U}}(t)$ is the velocity vector, $\boldsymbol{K}$ is the stiffness matrix, $\boldsymbol{U}(t)$ is the displacement vector and $\boldsymbol{F}$ is the external force vector. $\boldsymbol{C}$ of Eq. (1) was formulated by the stiffness-proportional damping matrix, and its coefficient was set to 0.01.

Eq. (1) is solved by the implicit method, the Newmark-β method is used in the time integration scheme, and a simultaneous linear equation is obtained as

$$\begin{aligned}\left(\frac{1}{\beta\Delta t^2}\boldsymbol{M} + \frac{\gamma}{\beta\Delta t}\boldsymbol{C} + \boldsymbol{K}\right)\boldsymbol{U}(t+\Delta t) = \boldsymbol{F} + \left(\frac{1}{\beta\Delta t^2}\boldsymbol{U}(t) + \frac{1}{\beta\Delta t}\dot{\boldsymbol{U}}(t) + \frac{1-2\beta}{2\beta}\ddot{\boldsymbol{U}}(t)\right)\boldsymbol{M} \\ + \left(\frac{\gamma}{\beta\Delta t}\boldsymbol{U}(t) + \frac{\gamma-\beta}{\beta}\dot{\boldsymbol{U}}(t) + \frac{\gamma-2\beta}{\beta}\Delta t\ddot{\boldsymbol{U}}(t)\right)\boldsymbol{C}\end{aligned} \tag{2}$$

where β and γ are the parameters, and were set to 0.25 and 0.50, respectively. The time interval Δt was set to be 0.005 sec, and the number of computational steps was 3,600.

The conjugate gradient (CG) method was applied for solving Eq. (2), and the symmetric successive over-relaxation (SSOR) pre-processing to the associated matrix was used. The threshold for determining iteratively the convergence of the relative error of computed displacement $\boldsymbol{U}(t)$ was set at 1.0×10^{-6}.

6 CHARACTERISTICS OF SEISMIC RESPONSE

The responses due to the action of the main motion for 10 sec from 8 to 18 sec are examined in the following sections, as previously stated that the analysis used site-specific waveforms acting for 18 sec from 0 to 18 sec.

6.1 Responses of abutments, piers and underground

Figure 6 shows the time history response waveforms of the relative displacements of piers P1–P4 tops to the base of each column $\boldsymbol{u}_{P.rel}$. Figure 7 shows the response trajectory of $\boldsymbol{u}_{P.rel}$ in the EW–NS plane. In Figure 7, we show the vectors for the maximum $\boldsymbol{u}_{P.rel}$.

From Figures 6 and 7, the maximum $\boldsymbol{u}_{P.rel}$ in the EW–NS plane are as follows. First, pier P2 shows 0.458 m to the west-northwest at 4.22 sec. Second, pier P3 shows 0.493 m to the southeast at 4.92 sec. Third, pier P1 shows 0.174 m to the east at 5.01 sec. Finally, pier P4 shows 0.549 m to the north-northwest at 7.11 sec. The drift ratio γ_P is obtained by dividing the $\boldsymbol{u}_{P.rel}$ by the pier height L. At first, the maximum γ_{P4} shows 3.43% for pier P4, and second, the maximum γ_{P2} shows 1.87% for pier P2. The values of γ_{P4} and γ_{P2} occur in the last and first phase in Figure 6. The maximum γ_{P1} and γ_{P3} for piers P1 and P3 show 1.74% and 1.64%,

respectively. The values of γ_{P1} and γ_{P3} occur between the occurrence time of γ_{P2} and γ_{P4}. Considering that the drift ratio of RC piers when they transition from the elastic to the plastic range is around 0.5%[11][12], it is highly likely that damage greater than cracking occurred around the pier bases at all piers.

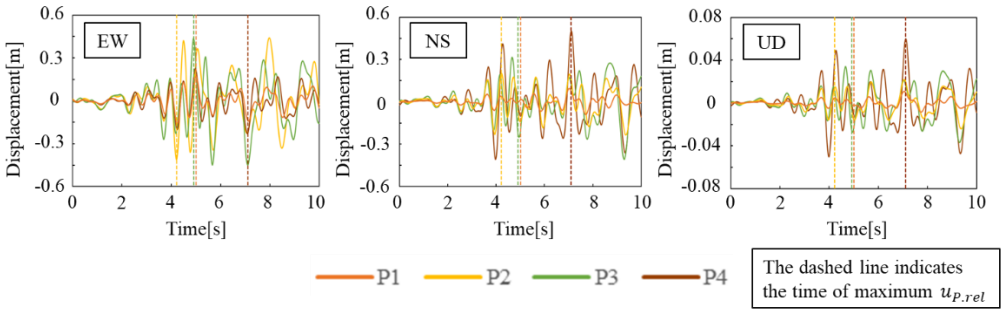

Figure 6: Relative displacement of piers P1–P4 tops to the base of each column

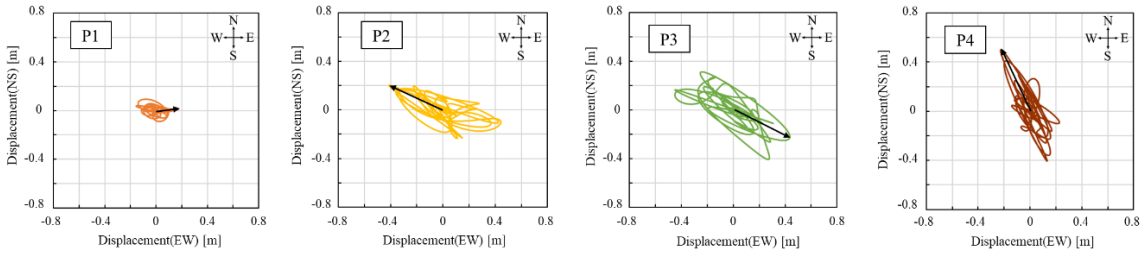

Figure 7: Response trajectory of relative displacement of piers P1–P4 tops to the base of each column

Figure 8 shows a contour diagram of the bridge structure-underground interconnected system at 5.0 sec, near the time of maximum γ_P at pier P3. The response of the underground from the contour diagram in Figure 8 shows that the underground between abutment A1 and pier P1, the underground near abutment A2 has a particularly large response, and the underground around pier P3 has a slightly larger response. Looking at the underground, where the response is large, the embankment layer between piers P2 and P3 is thicker, approximately 10 m. In addition, there is a layer of the pumice fall near abutment A1 and a layer of the non-welded tuff near abutment A2 at the surface, and these have a relatively low Young's modulus.

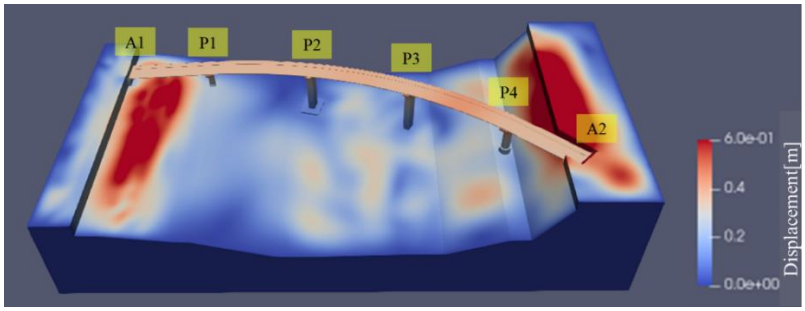

Figure 8: Contour plot of pier P3 at maximum response

6.2 Responses of laminated RBs and superstructure

Hereinafter, we focus on the middle RBs of the five RBs on each abutment and pier, and they will be represented as A[n]B for abutment A[n], n = 1,2 and P[m]B for pier P[m], m = 1,2,3,4.

Figure 9 shows the response trajectory of horizontal displacements of the RB on each abutment and pier in the EW–NS plane $\boldsymbol{u}_{B.rel}$. The horizontal displacements $\boldsymbol{u}_{B.rel}$ indicate the relative displacements of the upper RB to the lower RB. From Figure 9, the maximum $\boldsymbol{u}_{B.rel}$ are as follows. In descending order in the maximum $u_{B.rel}$, P4B shows 1.97 m to the south, A2B shows 1.58 m to the north, P3B shows 1.09 m to the south-southeast, P1B shows 1.08 m to the east-southeast, P2B shows 1.07 m to the northwest, and A1B shows 0.893 m to the south. The $\boldsymbol{u}_{B.rel}$ corresponding to the allowable shear strain of 250%[13] in the RBs on each abutment and pier are A1B: 0.30 m, P1B: 0.38 m, P2B: 0.21 m, P3B: 0.21 m, P4B: 0.35 m and A2B: 0.30 m. The shear strain of the RBs on all abutments and piers exceeds the allowable shear strain, indicating that the RBs on all abutments and piers reached the rupture zone.

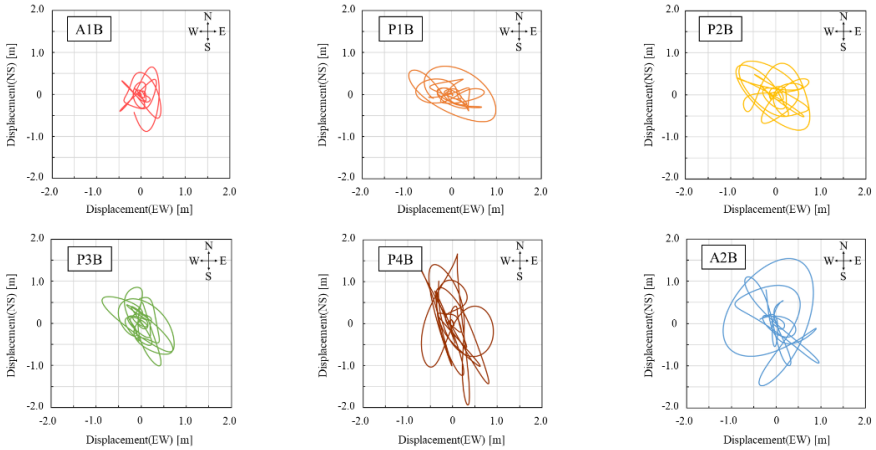

Figure 9: Response trajectory of horizontal displacements of RB on each abutment and pier

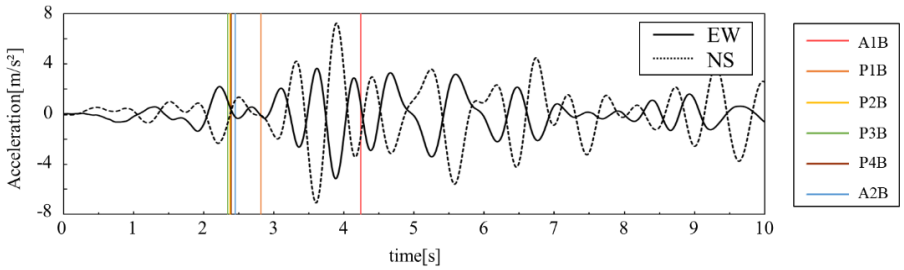

Figure 10: Relationship between time to reach allowable shear strain and site-specific waveforms

Figure 10 shows the relationship between the site-specific waveforms and the time when the RBs on each abutment and pier exceed the allowable shear strain of 250%. From Figure 10, the RBs exceed the allowable shear strain of 250% in P3B, P2B, P4B, A2B, P1B and A1B. The allowable shear strain tends to be reached from the RB on the high piers. P2B, P3B, P4B and A2B exceed the allowable shear strain almost synchronously in the early phase from 2.3 to 2.5

sec, following a pulse of acceleration of 2 m/s² for EW and NS. P1B and A1B are asynchronous with a time lag of 0.5 and 1.9 sec, respectively, after P3B exceeded the allowable shear strain. In A1B, the allowable shear strain is reached after the pulse at the peak of the site-specific waveforms at 3.9 sec. The following discussion focuses on the RB responses and superstructure behaviours before the peaks of the site-specific waveforms.

Figure 11 shows the response trajectory up to each time in Figure 9: Figure 11(a) depicts up to 2.8 sec when the RB on the P1 pier exceeds 250% allowable shear strain, and Figure 11(b) depicts up to 3.5 sec before the peaks of the site-specific waveforms. From Figure 11(a), up to 2.8 sec, the RB responses on all abutments and piers follow almost the same trajectory, anti-clockwise from northwest to southeast and then northwest to southeast. Thus, at the initial stage, the RB responses link to the uniform response of the underground shakings.

Looking at the response trajectory up to 3.5 sec shown in Figure 11(b), the RB responses on each abutment and pier are slightly different, with trajectories such as A1B: north to west, P1B: northwest to west, P2B: north to southwest, P3B: north to west, P4B: north to south, A2B: northeast to northwest. Figure 12 shows the response trajectory of the piers up to each time in Figure 7. Compared with the response trajectory of the piers, the RBs on all piers respond in the opposite phase to the responses of the piers at around 3.5 sec, before the peaks of the site-specific waveforms. Furthermore, the response trajectory of each pier is also slightly different near the peak of the site-specific waveforms in Figure 12(b).

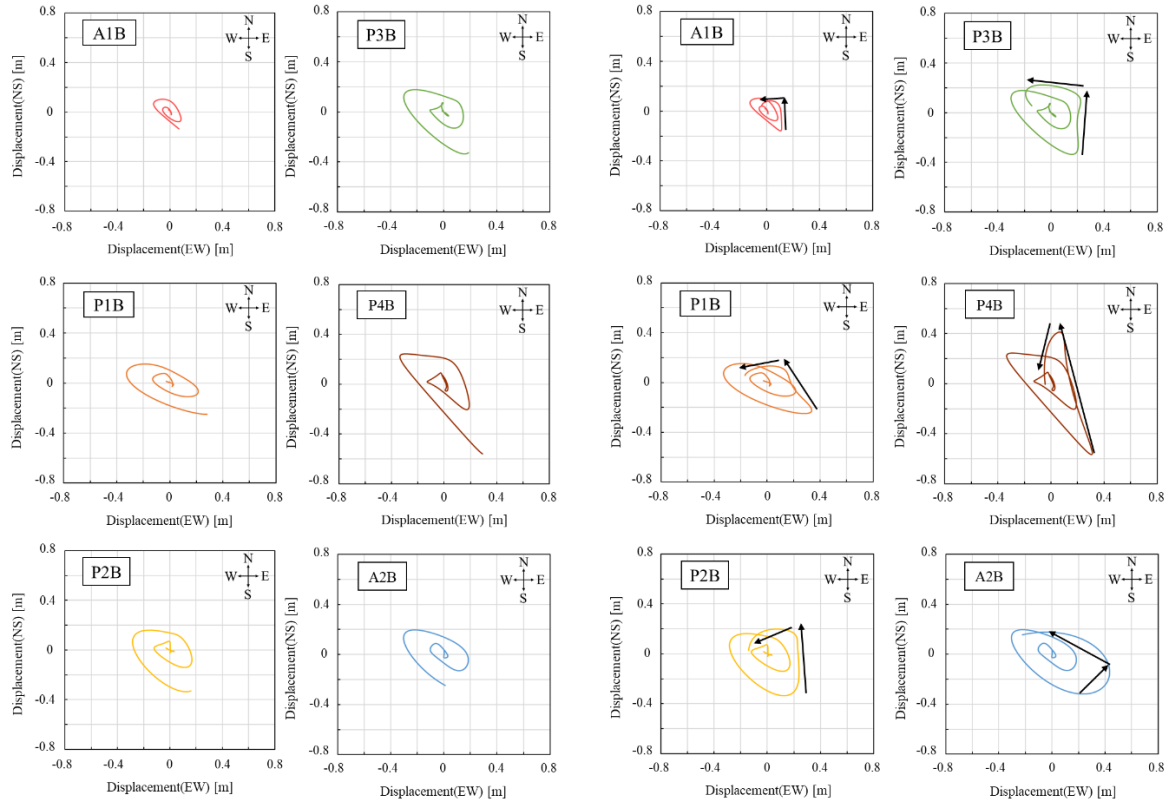

(a) Up to 2.8sec (b) Up to 3.5sec

Figure 11: Response trajectory horizontal displacements of RBs up to each time

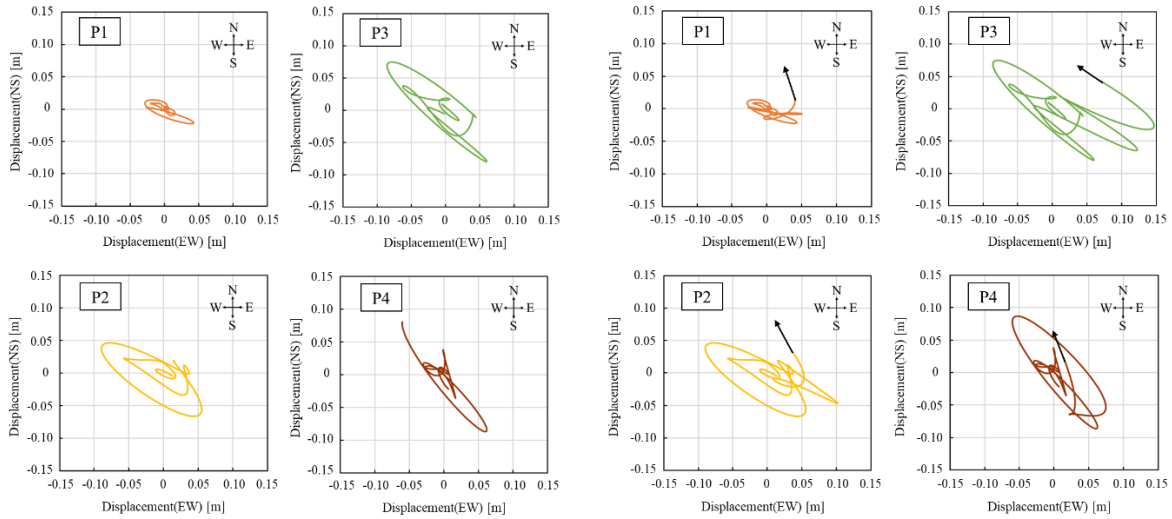

(a) Up to 2.8sec (b) Up to 3.5sec

Figure 12: Response trajectory of relative displacements of each pier top up to each time

From the final response trajectory in Figure 9, the trend of response in each abutment and pier is A1B: N–S, P1B: W–E, P2B: NW–SE, P3B: NW–SE, P4B: N–S, A2B: N–S. The above suggests that the response trajectory of the RBs are not very different at the initial stage in each abutment and pier. The response trajectory of the RBs differ from the vicinity of the peak of the site-specific waveforms coupled by opposite phase responses of the piers in Figure 12(b) and the unique responses of the underground around each abutment and pier in Figure 8.

Figure 13 shows the superstructure behaviours on each abutment and pier and the entire superstructure inferred from the coupled responses of RBs, abutments and piers obtained from this analysis. The entire superstructure seems to behave as follows: first, the superstructure moves to the northwest direction between 1.86 and 2.49 sec, then to the southeast direction between 2.49 and 2.82 sec with a slight clockwise rotation around abutment A1, and further to the north direction between 2.82 and 3.24 sec with an anti-clockwise rotation around abutment A1.

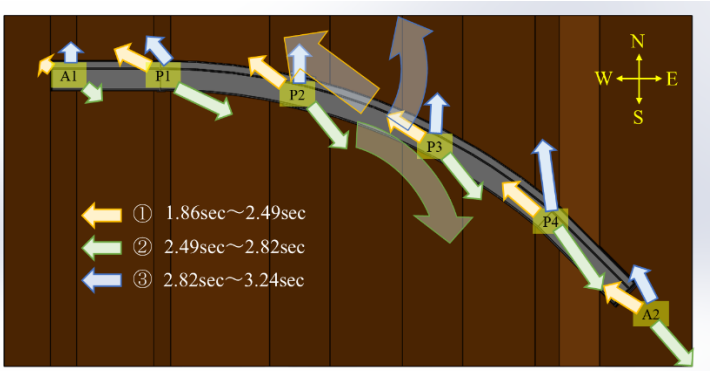

Figure 13: Estimated superstructure behaviours

7 CONCLUSIONS

(1) The response displacement of the site-specific waveforms estimated using the FD method shows a near-peak value near the first natural period of the Ohkirihata Bridge. Because these site-specific waveforms are the pulses from fault ruptures, we found that the pulses from fault ruptures contributed significantly to the response displacement of bridge structure-underground interconnected system of the Ohkirihata Bridge.

(2) Regarding the coupled responses of the superstructure, RBs, abutments, piers and underground during about 4 sec before the maximum amplitudes of the site-specific waveforms, we infer the following behaviours: first, the superstructure moves to the northwest direction, then to the southeast direction with a slight clockwise rotation around abutment A1, and further to the north direction with an anti-clockwise rotation around abutment A1.

ACKNOWLEDGMENTS

Kumamoto Reconstruction Project Office provided invaluable information on the structural characteristics of the Ohkirihata Bridge and the geotechnical properties of the underground. Assistant Professor Naoki Morita of the University of Tsukuba and other members of the FrontISTR Commons for their many helpful suggestions on FEM analysis. We express our deepest gratitude to everyone involved. The support received via JSPS KAKENHI Grant Number 19K21983 is gratefully acknowledged. This study was also motivated as supported by joint research between Public Works Research Institute and University of Tsukuba. The authors would like to thank MARUZEN-YUSHODO Co., Ltd.(https://kw.maruzen.co.jp/kousei-honyaku/) for English language editing.

REFERENCES

[1] Japan Meteorological Agency: Related information about the 2016 Kumamoto Earthquake, https://www.data.jma.go.jp/svd/eqev/data/2016_04_14_kumamoto/index.html, 10 Aug 2021.
[2] Japan Society of Civil Engineers (2017): Report on the Damage Surveys and Investigations Following the 2016 Kumamoto Earthquake, Chapter 4 Damage to road bridges.
[3] National Institute for Land and Infrastructure Management, Public Works Research Institute (2017): Report on Damage to Infrastructures by the 2016 Kumamoto Earthquake.
[4] Aoi, S. and Fujiwara, H. (1999): 3-D finite difference method using discontinuous grids, Bulletin of the Seismological Society of America, 89, 918-930.
[5] Asano, K. and Iwata, T. (2016): Source rupture processes of the foreshock and mainshock in the 2016 Kumamoto earthquake sequence estimated from the kinematic waveform inversion of strong motion data, Earth, Planets and Space, 68:147.
[6] Hara, M (2018): Relationship between and the seismic damage to buried sewer pipelines and input seismic motion, University of Tsukuba, Master's thesis.
[7] The Headquarters for Earthquake Research Promotion: Japan Integrated Velocity Structure Model, https://www.jishin.go.jp/main/chousa/12_choshuki/dat/, 6 Aug 2021.
[8] Japan Road Association (2017): Specifications for Highway Bridges Part V Seismic Design.
[9] Kasai, A., Yoshizuka, T. and Ushitsuka, Y. (2017): Damage analysis and FE model of the Ohkirihata Bridge in the 2016 Kumamoto earthquake, *Proceedings of the 20th Symposium on Performance-based Seismic Design Method for Bridges*, 449-456, Japan.
[10] FrontISTR: https://www.frontistr.com/, 10 Aug 2021.
[11] M. J. N. Priestley, F. Seible and G. M. Calvi (1996): Seismic Design and Retrofit of Bridges, Wiley-Interscience Publication.
[12] Nishida, H. and Unjoh, S. (2007): A study on engineering positioning of allowable plasticity factor of RC piers based on the specifications for highway bridges, *Proceedings of the 10th Symposium on Ductility Design Method for Bridges*, 249-254, Japan.
[13] Japan Road Association (2004): Bearings Handbook for Highway Bridges.